ACS APPLIED ELECTRONIC MATERIALS

pubs.acs.org/acsaelm Article

Combinatorial Approach for Single-Crystalline TaON Growth: Epitaxial β-TaON (100)/α-Al_2O_3 (012)

K. V. L. V. Narayanachari, D. Bruce Buchholz, Elise A. Goldfine, Jill K. Wenderott, Sossina M. Haile, and Michael J. Bedzyk*

Cite This: *ACS Appl. Electron. Mater.* 2020, 2, 3571–3576 Read Online

ABSTRACT: The photocatalyst β-TaON is of interest due to promising properties, such as stability, suitable band gap for visible light, and carrier mobility. We implemented a combinatorial, material discovery approach that used pulsed laser deposition (PLD) for thin-film growth, X-ray diffraction (XRD) for phase determination, and machine learning for data reduction. A lateral compositional gradient of TaO_xN_y was grown across the surface of an α-Al_2O_3 (012) wafer. After annealing, XRD scattering patterns were collected across the lateral gradient. Unsupervised machine learning separated the XRD data into four clusters (phases); one of which turned out to be the desired monoclinic β-TaON phase. Using high-resolution XRD, we determined that the β-TaON region of the film was a 260 Å thick single-crystal epitaxial with the substrate, having out-of-plane β-TaON (100)//α-Al_2O_3 (012) and in-plane β-TaON (010)//α-Al_2O_3 ($2\bar{1}0$). X-ray reflectivity (XRR) analysis of the β-TaON region of the film showed an electron density matching that expected for β-TaON. X-ray photoelectron spectroscopy (XPS) showed a Ta^{5+} valence state in the β-TaON region of the film. This combinatorial approach, which produces a library of phases on a single wafer, proved to be very efficient for the growth of a material's phase of interest.

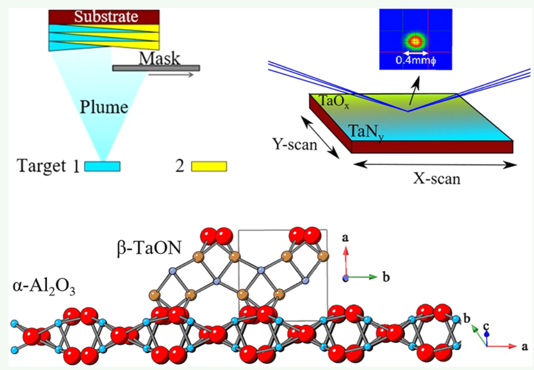

KEYWORDS: *β-TaON, combinatorial synthesis, thin film, PLD, XRD, machine learning*

■ INTRODUCTION

Increasing global energy demands and environmental concerns due to fossil fuel consumption obligates the search for renewable energy sources, such as solar energy, which is both clean and abundant. Among the various methods for solar energy conversion is the production of oxygen and hydrogen by water splitting. The use of semiconductor materials for overall water splitting (OWS) into O_2 and H_2 is an uphill reaction with a standard Gibb's free energy of 237 kJ mol^{-1} = 2.46 eV $molecule^{-1}$.[1−3] When the semiconductor absorbs a photon with an energy higher than the band gap, an electron is excited to the conduction band, leaving a hole in the valence band. The excited electrons and holes separately diffuse to the surface of the semiconductor and participate in oxidation and reduction reactions that produce oxygen and hydrogen.[4−6]

Since the first breakthrough of photocatalytic water splitting by Honda and Fujishima,[7] many semiconductor materials have been studied for this application. This includes transition metal oxides, along with oxynitrides, which are attracting much attention recently.[8−18] Many of the transition metal oxides are suitable materials due to abundance, stability, and nontoxicity, but their poor charge conductivity and wider band gaps result in lower efficiencies and the requirement of the higher energy/UV portion of the solar spectrum. Incorporation of nitrogen into the transition metal oxides is one way of reducing the band gap because of the shallow nature of the N 2p orbitals compared to the O 2p orbitals.[19−21]

Tantalum oxynitride with a monoclinic crystal structure (β-TaON) is a very attractive material for this photocatalytic application.[22,23] β-TaON has a band gap of 2.5 eV, which is within the visible part of the solar spectrum. The valence band maximum (VBM) and conduction band minimum (CBM) of this material are optimally positioned with respect to the reduction and oxidation potentials of the water-splitting reaction.[3,11,24]

Apart from the electronic structure of the photocatalytic material, the functionality strongly depends on the morphology of the material.[25,26] High-quality single-crystalline materials are required to reduce recombination centers (grain boundaries and other point defects) and to simplify the study of the structural and functional characteristics of the material. For example, the availability of single-crystalline TiO_2 made it possible to study the charge transport, recombination

Received: July 17, 2020
Accepted: October 15, 2020
Published: October 28, 2020

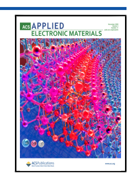

https://dx.doi.org/10.1021/acsaelm.0c00622
ACS Appl. Electron. Mater. 2020, 2, 3571−3576

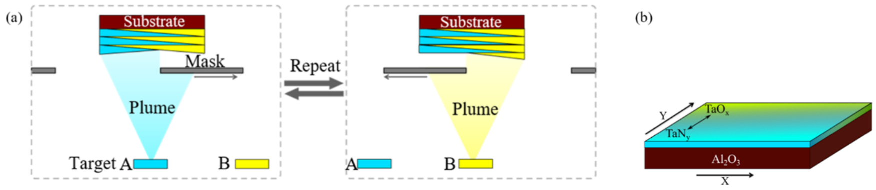

Figure 1. Depiction of the TaO_xN_y thin film grown by PLD on α-Al_2O_3(012). (a) Deposition of the TaO_x/TaN_y linear composition gradient film. (b) TaO_xN_y thin film with a composition gradient along the Y-direction and uniform along the X-direction.

mechanisms, and the effect of surface orientation on the photocatalytic activity.[27−29] Several attempts have been made to grow thin films of TaON using sputter deposition,[30−33] pulsed laser deposition (PLD),[34] and ammonolysis of Ta_2O_5.[1,35−37]

There are several crystalline phases of TaO_xN_y.[4,38] The 1:1:1 composition of TaON is known to exist in three polymorphs: monoclinic β-TaON ($P2_1/c$),[38,39] metastable γ-TaON ($C2/m$),[38,39] and δ-TaON ($I4_1/amd$).[40,41] Among these phases, β-TaON is semiconducting and the most stable. β-TaON is a baddeleyite-type structure and isostructural to ZrO_2.

To achieve single-crystal epitaxy of a desired film, a substrate needs to be chosen with a chemical and geometrical match at the film/substrate interface.[42] For β-TaON, r-plane sapphire (α-Al_2O_3 (012)) was chosen, which has a pseudo rectangular surface unit cell with lattice constants a_s = 5.13 Å and b_s = 4.76 Å that reasonably match the rectangular surface unit cell of β-TaON (100) with lattice constants a_s = 5.19 Å and b_s = 5.04 Å.

For efficiency, our material development process combined a compositional spread in the synthesis step with high-throughput measurements of the produced phases.[43−46] Machine learning-based big data techniques were used to convert a large set of experimental data into actionable small clusters.[47−50] In the process of trying to grow a β-TaON thin film, the stoichiometry (O/N) is crucial to obtaining the preferred phase.[24] Instead of realizing and optimizing the O/N ratio from a large set of individual thin-film samples, we deposited a lateral compositional graded thin-film sample using multitarget PLD.[51] Ideally, the composition should range from TaN at one edge of the substrate to Ta_2O_5 at the opposite edge. The use of high-throughput, small-area X-ray diffraction (XRD) measurements combined with machine learning-based analysis made it possible to identify the desired β-TaON phase on the compositionally graded sample.

■ EXPERIMENTAL METHODS

α-Al_2O_3 (012) (r-plane sapphire) substrates (25 × 25 mm^2) were precleaned with acetone and isopropanol before the introduction into the PVD Products PLD/MBE 2300 chamber, where the TaO_x/TaN_y linear composition gradient films were grown on the substrates by PLD (see Figure 1).

The PLD system uses a 248 nm KrF excimer laser with a 25 ns pulse duration. The dense hot-pressed PLD targets of Ta_2O_5 and TaN were purchased from Kurt J. Lesker Company. The deposition ambient was 10 mTorr N_2, and the substrate deposition temperature was 675 °C.

The laterally graded film was obtained using an alternating layer-by-layer technique in combination with a traveling mask.[43] Each TaO_x layer was deposited using 100 laser pulses from the Ta_2O_5 target, while the mask swept laterally across the substrate in 20 s (see Figure 1a). Similarly, each TaN_y layer was deposited using 300 laser pulses from the TaN target, while the mask swept in the opposite direction across the substrate in 20 s. The thicknesses of individual layers at the two extreme lateral ends, where the composition was 100% TaO_x or 100% TaN_y, were 1−2 Å. The process of alternating between TaO_x and TaN_y wedge-shaped layers was repeated 150 times. A detailed description is included in the Supporting Information. After deposition, the thin-film sample was annealed in a tube furnace at 1000 °C for 2 h in nitrogen (99.999%) at ambient pressure to promote grain growth. Based on X-ray reflectivity (XRR), the total film thickness was 260 Å at the TaN_y and 160 Å at the TaO_x end of the compositional gradient.

Small-area X-ray diffraction (XRD) measurements used a 3 KW Cu target Rigaku Smartlab with a polycapillary optic (CBO-f unit) that focused the line source from the X-ray anode to a spot of 400 μm diameter at the sample. A two-dimensional (2D) HyPix 3000 detector was used to collect the scattering patterns in a $\theta/2\theta$ specular reflection geometry. (See Figure S2 for the X-ray experimental setup.) The 2D scattering pattern was converted to a one-dimensional (1D) function $I(Q)$, where the modulus of the scattering vector $Q = 4\pi \sin(\theta)/\lambda$, 2θ is the scattering angle, and λ is the X-ray wavelength. The sample was aligned in the incident beam direction to minimize the X-ray footprint in the composition gradient direction (Y-direction) to a value of 400 μm. Data were collected in 71 steps along this direction. To determine the in-plane epitaxial orientation of the film relative to the substrate lattice, we used parallel beam optics from a 9 KW Cu rotating anode SmartLab to find the χ and ϕ angles at which off-specular reflections occurred for the substrate and film. Tilt angle χ is the angle between the desired off-specular hkl reciprocal space vector and the Al_2O_3 (012) vector. Angle ϕ is the azimuthal rotation about the Al_2O_3 (012) vector. For increasing the in-plane resolution, 0.5° soller slits were used on the incident and detector arms of the diffractometer. The incident beam slits limited the beam width to a 3 mm wide footprint on the sample centered at the location of interest. This same 9 KW SmartLab was also used for the specular low-angle X-ray reflectivity measurements.

■ RESULTS AND DISCUSSION

Figure 2a shows the specular X-ray scattered intensity as a function of Q_z and lateral position (Y) along the compositional gradient direction with a pitch of 350 μm.

Using fuzzy c-means (FCM) clustering, we developed a Python code for clustering the XRD data based on the similarity of the diffraction patterns.[52] Using unsupervised machine learning, all of the XRD patterns were grouped into four clusters (see the Supporting Information for details on clustering). Peak positions from each cluster are compared to patterns in the International Centre for Diffraction Data-Powder Diffraction File (ICDD-PDF) database and matched to Ta_2O_5 and TaON phases, as shown in Figure 3. In particular, cluster 0, which extends from Y = −12.5 to −6 mm, encompassing the nitrogen-rich region of the composition gradient, is dominated by β-TaON. Only a very minor contribution from Ta_2O_5 is evident in this cluster. In contrast, clusters 1, 2, and 3 are all largely described by Ta_2O_5, with discrepancies due to differences in crystallinity and orientation. Because of peak overlap in the XRD data, the presence of nitride phases (TaN, Ta_3N_5) cannot be ruled out. However, as shown in Figure S6, we can rule out these phases based on XPS analysis. Rietveld refinement of the specular XRD data on the nitrogen-rich end of the gradient shows that the pattern can be

https://dx.doi.org/10.1021/acsaelm.0c00622
ACS Appl. Electron. Mater. 2020, 2, 3571−3576

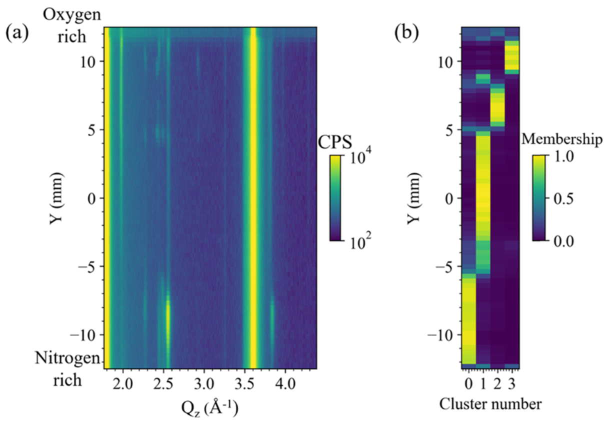

Figure 2. Focused beam XRD data. (a) Specular XRD intensities $I(Q)$ collected as a function of Y along the composition gradient of the film. The highest intensities at Q_Z = 1.81 and 3.61 Å^{-1} are from the Al_2O_3 (012) and (024) Bragg peaks. (b) XRD patterns from the film are separated into four clusters by unsupervised machine learning. Membership represents the probability of a pattern belonging to a cluster.

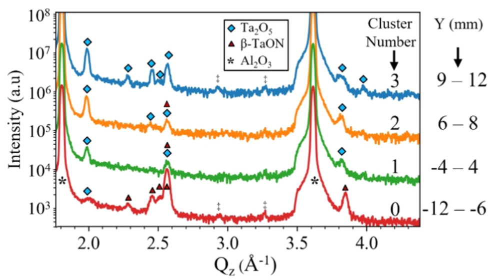

Figure 3. Representative XRD intensity patterns from Figure 2 for the four clusters with identified peaks from the Ta_2O_5 and TaON phases. The peaks in cluster 0 at Q_Z = 2.57 and 3.84 Å^{-1} correspond to the β-TaON (200) and (300) planes, respectively. The high-intensity peaks at 1.81 and 3.61 Å^{-1} are from the single-crystal substrate α-Al_2O_3 (012) and (024) planes, respectively. Each XRD intensity curve is offset by 1 decade for purposes of clarity. ‡ refers to unidentified peaks.

described as 99% β-TaON with a trace amount of Ta_2O_5 (see Figure S5). Even on the nitrogen-rich end, there is substantial oxygen incorporation that occurred during film growth from TaN PLD target and/or postgrowth annealing.

The relatively high intensities from the (200) and (300) peaks of β-TaON in cluster 0 at Q_z = 2.57 and 3.84 Å^{-1} point to the possibility of texture or single-crystal epitaxy in the (100) direction. To evaluate this possibility, we performed additional diffraction studies (Figures 4 and 5) probing an area of the film entirely within cluster 0, i.e., centered at Y = −8.7 mm, using a parallel beam X-ray setup with a beam width of 3 mm along the Y-direction.

We performed a higher-resolution longitudinal Q_z scan (Figure 4a) and a transverse Q_x scan (Figure 4b) through the (200) peak. The calculated crystallite sizes in lateral and normal directions on the film, from FWHM of the Q_z and Q_x, are 251 and 105 Å, respectively. The narrow width of the substrate rocking curve, as shown in Figure 4c, confirms that the broadening of the film peaks was not due to instrument resolution. To explore if the peak in the Q_x scan (Figure 4b) indicates single-crystal epitaxy or just texture; we performed φ-scans at the off-specular β-TaON (130), (11$\bar{1}$), and (110) Bragg conditions (see Figure 5a). Comparing the peak positions in these φ-scans to that of the α-Al_2O_3 (113) indicates that the film is epitaxial with out-of-plane β-TaON (100)//α-Al_2O_3 (012) and in-plane β-TaON (010)//α-Al_2O_3 (2$\bar{1}$0). The stereographic projection of the *hkl* poles in Figure 5b helps explain the directional relationships between the two lattices.

For the case of single-crystal β-TaON (100) only, two peaks are expected in a φ-scan of the (11$\bar{1}$) reflection (shown in Figure 5b separated by Δφ = 91.6°), whereas four peaks are present in the experiment (see Figure 5a). This is due to nucleation and growth leading to two morphologically equivalent in-plane orientations for β-TaON (100)/α-Al_2O_3(012), one orientation with β-TaON(010)//α-Al_2O_3(100) and the other orientation with β-TaON(0$\bar{1}$0)//α-Al_2O_3(100) as represented in Figure 6b. As a result of this twinning, a mirror symmetry in the φ-scan of (11$\bar{1}$) poles is observed instead of just two peaks separated by 91.6°.

After confirming the β-TaON crystalline phase presence and epitaxial relations, the β-TaON density was compared to that of the bulk crystal. A low-angle X-ray reflectivity (XRR) measurement was performed at the location of the β-TaON on the compositionally graded sample using a parallel beam setup with an X-ray beam width of 3 mm. As shown in Figure 7, along with the fit to the XRR, data determines the electron density profile.[53] From this fit, we find a film thickness of 260 Å and electron densities that match the expected bulk values of 2.65 and 1.19 e Å^{-3} for β-TaON and α-Al_2O_3, respectively. The film thickness closely matches the out-of-plane single-crystal domain size of 251 Å obtained from Figure 4a Q_z scan, further confirming the single-crystal nature of the film in this region.

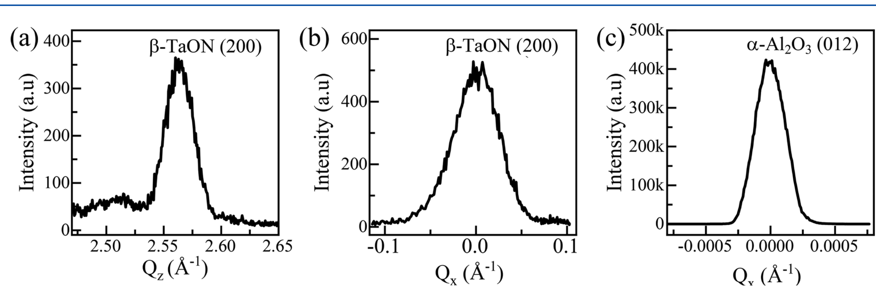

Figure 4. Parallel beam XRD data from the location centered at Y = −8.65 mm (with a breadth of 3 mm). (a) β-TaON (200) peak from θ/2θ scan with a full width at half-maximum (FWHM) ΔQ_z = 0.025 Å^{-1}, which corresponds to an out-of-plane single-crystal domain size D_Z = 251 Å. (b) β-TaON (200) peak from ω-scan with FWHM ΔQ_x = 0.06 Å^{-1}, corresponds to in-plane single-crystal domain size D_X = 105 Å. (c) ω-scan of α-Al_2O_3 (012) with FWHM ΔQ_x = 0.00027 Å^{-1}, corresponds to diffractometer resolution.

https://dx.doi.org/10.1021/acsaelm.0c00622
ACS Appl. Electron. Mater. 2020, 2, 3571−3576

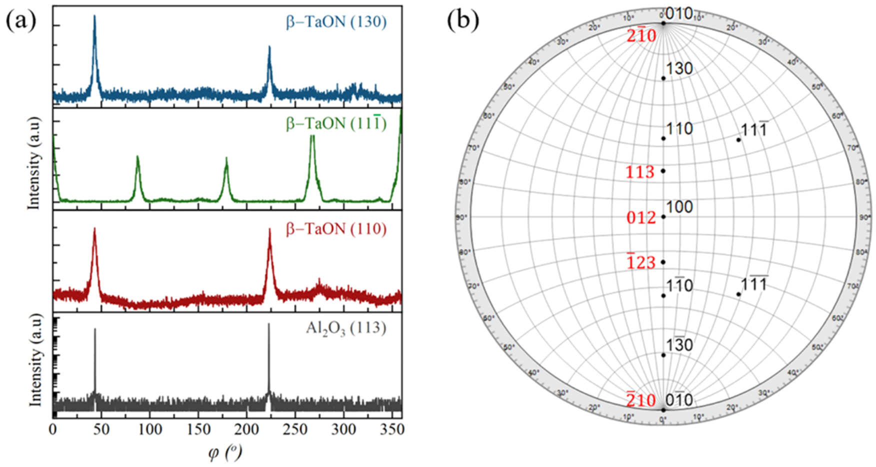

Figure 5. Local XRD measurements on the graded sample at $Y = -8.65$ mm, using a parallel beam setup with an X-ray beam width of 3 mm. (a) φ-Scans representing in-plane orientation relation between the substrate (113) and the single-crystalline β-TaON film. (b) Stereographic projection of *hkl* poles for β-TaON (black labels) and α-Al_2O_3 (red labels) with β-TaON (100)//α-Al_2O_3 (012) and β-TaON (010)//α-Al_2O_3 ($2\bar{1}0$).

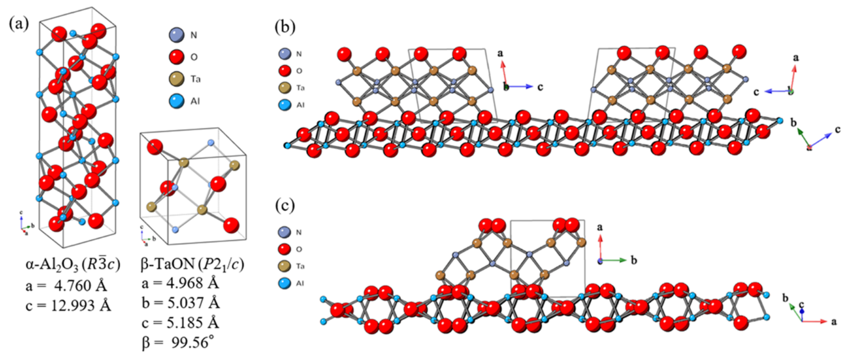

Figure 6. (a) Unit cells of α-Al_2O_3 and monoclinic β-TaON. (b) Projection of β-TaON (100)/α-Al_2O_3 (012) epitaxial relation along the film $-b$-axis direction (left), $+b$-axis direction (right), which are parallel to the substrate *a*-axis direction. (c) Same as (b), but projection along the film $+c$-axis direction, which is along the substrate [12−1] direction.

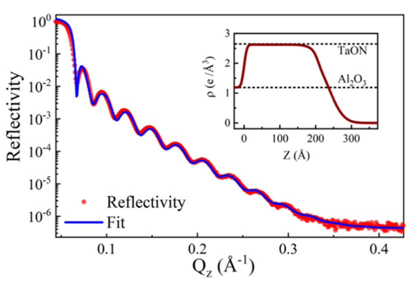

Figure 7. Specular XRR data (solid circles) and best fit for the β-TaON (260 Å thickness) on α-Al_2O_3. Inset is the electron density profile determined from the reflectivity fit. Expected densities for the TaON and α-Al_2O_3 are shown as dotted lines. XRR was measured at the β-TaON phase location, $Y = -8.65$ mm.

■ CONCLUSIONS

In summary, PLD film growth from TaN and Ta_2O_5 end members and high-throughput XRD characterization combined with machine learning-based data reduction techniques made the identification of epitaxial β-TaON(100)/α-Al_2O_3(012) possible in an efficient manner. Small-area X-ray diffraction and XPS studies showed β-TaON as the dominant phase at the nitrogen-rich end of the film, with Ta_2O_5 occurring at the oxygen-rich end. X-ray φ-scans of the off-specular reflections from the film and substrate at a β-TaON dominated position showed the epitaxial relation β-TaON (100)//α-Al_2O_3 (012) and β-TaON (010)//α-Al_2O_3 ($2\bar{1}0$). A fit to the specular XRR reflectivity (at this same position) yielded a film thickness of 260 Å and a calculated electron density of 2.63 e Å^{-3}, matching with the expected value 2.65 e Å^{-3} for β-TaON. Our results indicate that graded film synthesis, in tandem with high-throughput XRD and machine learning tools, provides a novel approach to effectively and efficiently identify synthesis routes to desired materials.

■ ASSOCIATED CONTENT

Supporting Information

The Supporting Information is available free of charge at https://pubs.acs.org/doi/10.1021/acsaelm.0c00622.

Detailed synthesis methods for composition gradient, description of small-area XRD setup, specular XRD of as-deposited and annealed films, details of ML-based clustering, and Rietveld refinement of GI-XRD data (PDF)

■ AUTHOR INFORMATION

Corresponding Author

Michael J. Bedzyk − *Department of Materials Science and Engineering and Department of Physics and Astronomy, Northwestern University, Evanston, Illinois 60208, United*

https://dx.doi.org/10.1021/acsaelm.0c00622
ACS Appl. Electron. Mater. 2020, 2, 3571−3576

States; orcid.org/0000-0002-1026-4558; Email: bedzyk@northwestern.edu

Authors

K. V. L. V. Narayanachari – *Department of Materials Science and Engineering, Northwestern University, Evanston, Illinois 60208, United States;* orcid.org/0000-0002-2033-8717

D. Bruce Buchholz – *Department of Materials Science and Engineering, Northwestern University, Evanston, Illinois 60208, United States*

Elise A. Goldfine – *Department of Materials Science and Engineering, Northwestern University, Evanston, Illinois 60208, United States*

Jill K. Wenderott – *Department of Materials Science and Engineering, Northwestern University, Evanston, Illinois 60208, United States*

Sossina M. Haile – *Department of Materials Science and Engineering, Northwestern University, Evanston, Illinois 60208, United States;* orcid.org/0000-0002-5293-6252

Complete contact information is available at:
https://pubs.acs.org/10.1021/acsaelm.0c00622

Notes

The authors declare no competing financial interest.

■ ACKNOWLEDGMENTS

This research was primarily supported by the US National Science Foundation (NSF) MRSEC Program (DMR-1720139) at Northwestern University (NU). This work made use of the X-Ray Diffraction, Pulsed Laser Deposition, and Keck-II facilities at NU supported by the MRSEC program of the (NSF DMR-1720139), Keck Foundation, State of Illinois, and the Soft and Hybrid Nanotechnology Experimental (SHyNE) Resource (NSF ECCS-1542205).

■ REFERENCES

(1) Bae, S. T.; Shin, H.; Lee, S.; Kim, D. W.; Jung, H. S.; Hong, K. S. Visible-light photocatalytic activity of NH_3-heat-treated Ta_2O_5 to decompose rhodamine B in aqueous solution. *React. Kinet., Mech. Catal.* **2012**, *106*, 67.

(2) Chen, S.; Takata, T.; Domen, K. Particulate photocatalysts for overall water splitting. *Nat. Rev. Mater.* **2017**, *2*, No. 17050.

(3) Kudo, A.; Miseki, Y. Heterogeneous photocatalyst materials for water splitting. *Chem. Soc. Rev.* **2009**, *38*, 253−278.

(4) Ullah, H.; Tahir, A. A.; Bibi, S.; Mallick, T. K.; Karazhanov, S. Z. Electronic properties of β-TaON and its surfaces for solar water splitting. *Appl. Catal., B* **2018**, *229*, 24−31.

(5) Chun, W. J.; Ishikawa, A.; Fujisawa, H.; Takata, T.; Kondo, J. N.; Hara, M.; Kawai, M.; Matsumoto, Y.; Domen, K. Conduction and valence band positions of Ta_2O_5, TaON, and Ta_3N_5 by UPS and electrochemical methods. *J. Phys. Chem. B* **2003**, *107*, 1798−1803.

(6) Takata, T.; Hitoki, G.; Kondo, J. N.; Hara, M.; Kobayashi, H.; Domen, K. Visible-light-driven photocatalytic behavior of tantalum-oxynitride and nitride. *Res. Chem. Intermed.* **2007**, *33*, 13−25.

(7) Fujishima, A.; Honda, K. Electrochemical photolysis of water at a semiconductor electrode. *Nature* **1972**, *238*, 37−38.

(8) Hisatomi, T.; Domen, K. Introductory lecture: sunlight-driven water splitting and carbon dioxide reduction by heterogeneous semiconductor systems as key processes in artificial photosynthesis. *Faraday Discuss.* **2017**, *198*, 11−35.

(9) Wang, Q.; Hisatomi, T.; Jia, Q.; Tokudome, H.; Zhong, M.; Wang, C.; Pan, Z.; Takata, T.; Nakabayashi, M.; Shibata, N.; Li, Y.; Sharp, I. D.; Kudo, A.; Yamada, T.; Domen, K. Scalable water splitting on particulate photocatalyst sheets with a solar-to-hydrogen energy conversion efficiency exceeding 1. *Nat. Mater.* **2016**, *15*, 611−615.

(10) Pan, C.; Takata, T.; Domen, K. Overall Water Splitting on the Transition-Metal Oxynitride Photocatalyst $LaMg_{1/3}Ta_{2/3}O_2N$ over a Large Portion of the Visible-Light Spectrum. *Chem. − Eur. J.* **2016**, *22*, 1854−1862.

(11) Takata, T.; Pan, C.; Domen, K. Recent progress in oxynitride photocatalysts for visible-light-driven water splitting. *Sci. Technol. Adv. Mater.* **2015**, *16*, No. 033506.

(12) Pan, C.; Takata, T.; Nakabayashi, M.; Matsumoto, T.; Shibata, N.; Ikuhara, Y.; Domen, K. A complex perovskite-type oxynitride: the first photocatalyst for water splitting operable at up to 600 nm. *Angew. Chem., Int. Ed.* **2015**, *54*, 2955−2959.

(13) Landsmann, S.; Maegli, A. E.; Trottmann, M.; Battaglia, C.; Weidenkaff, A.; Pokrant, S. Design Guidelines for High-Performance Particle-Based Photoanodes for Water Splitting: Lanthanum Titanium Oxynitride as a Model. *ChemSusChem* **2015**, *8*, 3451−3458.

(14) Abe, R.; Higashi, M.; Domen, K. Facile fabrication of an efficient oxynitride TaON photoanode for overall water splitting into H_2 and O_2 under visible light irradiation. *J. Am. Chem. Soc.* **2010**, *132*, 11828−11829.

(15) Yang, J.; Wang, D.; Han, H.; Li, C. Roles of cocatalysts in photocatalysis and photoelectrocatalysis. *Acc. Chem. Res.* **2013**, *46*, 1900−1909.

(16) Chu, S.; Majumdar, A. Opportunities and challenges for a sustainable energy future. *Nature* **2012**, *488*, 294−303.

(17) Cui, Z. H.; Jiang, H. Theoretical Investigation of Ta_2O_5, TaON, and Ta_3N_5: Electronic Band Structures and Absolute Band Edges. *J. Phys. Chem. C* **2017**, *121*, 3241−3251.

(18) de Respinis, M.; Fravventura, M.; Abdi, F. F.; Schreuders, H.; Savenije, T. J.; Smith, W. A.; Dam, B.; van de Krol, R. Oxynitrogenography: Controlled Synthesis of Single-Phase Tantalum Oxynitride Photoabsorbers. *Chem. Mater.* **2015**, *27*, 7091−7099.

(19) Xiao, M.; Wang, S. C.; Thaweesak, S.; Luo, B.; Wang, L. Z. Tantalum (Oxy)Nitride: Narrow Bandgap Photocatalysts for Solar Hydrogen Generation. *Engineering* **2017**, *3*, 365−378.

(20) Fang, C. M.; Orhan, E.; de Wijs, G. A.; Hintzen, H. T.; de Groot, R. A.; Marchand, R.; Saillard, J. Y.; de With, G. The electronic structure of tantalum (oxy)nitrides TaON and Ta_3N_5. *J. Mater. Chem.* **2001**, *11*, 1248−1252.

(21) Harb, M.; Sautet, P.; Nurlaela, E.; Raybaud, P.; Cavallo, L.; Domen, K.; Basset, J. M.; Takanabe, K. Tuning the properties of visible-light-responsive tantalum (oxy)nitride photocatalysts by non-stoichiometric compositions: a first-principles viewpoint. *Phys. Chem. Chem. Phys.* **2014**, *16*, 20548−20560.

(22) Ahmed, M.; Xinxin, G. A review of metal oxynitrides for photocatalysis. *Inorg. Chem. Front.* **2016**, *3*, 578−590.

(23) Sakar, M.; Prakash, R. M.; Shinde, K.; Balakrishna, G. R. Revisiting the materials and mechanism of metal oxynitrides for photocatalysis. *Int. J. Hydrogen Energy* **2020**, *45*, 7691−7705.

(24) Salamon, K.; Micetic, M.; Sancho-Parramon, J.; Radovic, I. B.; Siketic, Z.; Saric, I.; Petravic, M.; Bernstorff, S. TaON thin films: production by reactive magnetron sputtering and the question of non-stoichiometry. *J. Phys. D: Appl. Phys.* **2019**, *52*, No. 305304.

(25) Pinaud, B. A.; Vesborg, P. C. K.; Jaramillo, T. F. Effect of Film Morphology and Thickness on Charge Transport in Ta_3N_5/Ta Photoanodes for Solar Water Splitting. *J. Phys. Chem. C* **2012**, *116*, 15918−15924.

(26) Tsang, M. Y.; Pridmore, N. E.; Gillie, L. J.; Chou, Y. H.; Brydson, R.; Douthwaite, R. E. Enhanced photocatalytic hydrogen generation using polymorphic macroporous TaON. *Adv. Mater.* **2012**, *24*, 3406−3409.

(27) Chen, H.; Nanayakkara, C. E.; Grassian, V. H. Titanium dioxide photocatalysis in atmospheric chemistry. *Chem. Rev.* **2012**, *112*, 5919−5948.

(28) Tao, J. G.; Batzill, M. Role of Surface Structure on the Charge Trapping in TiO_2 Photocatalysts. *J. Phys. Chem. Lett.* **2010**, *1*, 3200−3206.

(29) Tao, J.; Luttrell, T.; Bylsma, J.; Batzill, M. Adsorption of Acetic Acid on Rutile TiO_2(110) vs (011)-2 × 1 Surfaces. *J. Phys. Chem. C* **2011**, *115*, 3434−3442.

https://dx.doi.org/10.1021/acsaelm.0c00622
ACS Appl. Electron. Mater. 2020, 2, 3571−3576

(30) Cristea, D.; Cunha, L.; Gabor, C.; Ghiuta, I.; Croitoru, C.; Marin, A.; Velicu, L.; Besleaga, A.; Vasile, B. Tantalum Oxynitride Thin Films: Assessment of the Photocatalytic Efficiency and Antimicrobial Capacity. *Nanomaterials* **2019**, *9*, No. 476.
(31) Khemasiri, N.; Jessadaluk, S.; Chananonnawathorn, C.; Vuttivong, S.; Lertvanithphol, T.; Horprathum, M.; Eiamchai, P.; Patthanasettakul, V.; Klamchuen, A.; Pankiew, A.; Porntheeraphat, S.; Nukeaw, J. Optical band engineering of metal-oxynitride based on tantalum oxide thin film fabricated via reactive gas-timing RF magnetron sputtering. *Surf. Coat. Technol.* **2016**, *306*, 346−350.
(32) Rezek, J.; Vlcek, J.; Houska, J.; Cerstvy, R. High-rate reactive high-power impulse magnetron sputtering of Ta−O−N films with tunable composition and properties. *Thin Solid Films* **2014**, *566*, 70−77.
(33) Tao, J.; Chai, J. W.; Wong, L. M.; Zhang, Z.; Pan, J. S.; Wang, S. J. Growth of single crystalline TaON on yttria-stabilized zirconia (YSZ). *J. Solid State Chem.* **2013**, *204*, 27−31.
(34) Lahoz, R.; Espinós, J. P.; Yubero, F.; Gonzalez-Elipe, A. R.; de la Fuente, G. F. "In situ" XPS studies of laser-induced surface nitridation and oxidation of tantalum. *J. Mater. Res.* **2015**, *30*, 2967−2976.
(35) Allam, N. K.; Shaheen, B. S.; Hafez, A. M. Layered tantalum oxynitride nanorod array carpets for efficient photoelectrochemical conversion of solar energy: experimental and DFT insights. *ACS Appl. Mater. Interfaces* **2014**, *6*, 4609−4615.
(36) Dabirian, A.; van de Krol, R. High-Temperature Ammonolysis of Thin Film Ta_2O_5Photoanodes: Evolution of Structural, Optical, and Photoelectrochemical Properties. *Chem. Mater.* **2015**, *27*, 708−715.
(37) de Respinis, M.; Fravventura, M.; Abdi, F. F.; Schreuders, H.; Savenije, T. J.; Smith, W. A.; Dam, B.; van de Krol, R. Oxynitrogenography: Controlled Synthesis of Single-Phase Tantalum Oxynitride Photoabsorbers. *Chem. Mater.* **2015**, *27*, 7091−7099.
(38) Wolff, H.; Bredow, T.; Lerch, M.; Schilling, H.; Irran, E.; Stork, A.; Dronskowski, R. A first-principles study of the electronic and structural properties of gamma-TaON. *J. Phys. Chem. A* **2007**, *111*, 2745.
(39) Schilling, H.; Stork, A.; Irran, E.; Wolff, H.; Bredow, T.; Dronskowski, R.; Lerch, M. Gamma-TaON: a metastable polymorph of tantalum oxynitride. *Angew. Chem., Int. Ed.* **2007**, *46*, 2931−2934.
(40) Lüdtke, T.; Schmidt, A.; Göbel, C.; Fischer, A.; Becker, N.; Reimann, C.; Bredow, T.; Dronskowski, R.; Lerch, M. Synthesis and crystal structure of δ-TaON, a metastable polymorph of tantalum oxide nitride. *Inorg. Chem.* **2014**, *53*, 11691−11698.
(41) Lüdtke, T.; Weber, D.; Schmidt, A.; Müller, A.; Reimann, C.; Becker, N.; Bredow, T.; Dronskowski, R.; Ressler, T.; Lerch, M. Synthesis and characterization of metastable transition metal oxides and oxide nitrides. *Z. Kristallogr. − Cryst. Mater.* **2017**, *232*, 3−14.
(42) O'Sullivan, M.; Hadermann, J.; Dyer, M. S.; Turner, S.; Alaria, J.; Manning, T. D.; Abakumov, A. M.; Claridge, J. B.; Rosseinsky, M. J. Interface control by chemical and dimensional matching in an oxide heterostructure. *Nat. Chem.* **2016**, *8*, 347−353.
(43) Koinuma, H.; Takeuchi, I. Combinatorial solid-state chemistry of inorganic materials. *Nat. Mater.* **2004**, *3*, 429−438.
(44) Takeuchi, I.; Yang, W.; Chang, K.; Aronova, M.; Venkatesan, T.; Vispute, R.; Bendersky, L. Monolithic multichannel ultraviolet detector arrays and continuous phase evolution in Mg_x $Zn_{1-x}O$ composition spreads. *J. Appl. Phys.* **2003**, *94*, 7336−7340.
(45) Fukumura, T.; Ohtani, M.; Kawasaki, M.; Okimoto, Y.; Kageyama, T.; Koida, T.; Hasegawa, T.; Tokura, Y.; Koinuma, H. Rapid construction of a phase diagram of doped Mott insulators with a composition-spread approach. *Appl. Phys. Lett.* **2000**, *77*, 3426−3428.
(46) Suram, S. K.; Fackler, S. W.; Zhou, L.; N'Diaye, A. T.; Drisdell, W. S.; Yano, J.; Gregoire, J. M. Combinatorial Discovery of Lanthanum−Tantalum Oxynitride Solar Light Absorbers with Dilute Nitrogen for Solar Fuel Applications. *ACS Comb. Sci.* **2018**, *20*, 26−34.
(47) Pilania, G.; Wang, C. C.; Jiang, X.; Rajasekaran, S.; Ramprasad, R. Accelerating materials property predictions using machine learning. *Sci. Rep.* **2013**, *3*, No. 2810.
(48) Saad, Y.; Gao, D.; Ngo, T.; Bobbitt, S.; Chelikowsky, J. R.; Andreoni, W. Data mining for materials: Computational experiments with A B compounds. *Phys. Rev. B* **2012**, *85*, No. 104104.
(49) Mueller, T.; Kusne, A. G.; Ramprasad, R. Machine Learning in Materials Science: Recent Progress and Emerging Applications. *Rev. Comput. Chem.* **2016**, *29*, 186−273.
(50) Long, C. J.; Hattrick-Simpers, J.; Murakami, M.; Srivastava, R. C.; Takeuchi, I.; Karen, V. L.; Li, X. Rapid structural mapping of ternary metallic alloy systems using the combinatorial approach and cluster analysis. *Rev. Sci. Instrum.* **2007**, *78*, No. 072217.
(51) Takeuchi, I.; van Dover, R. B.; Koinuma, H. Combinatorial synthesis and evaluation of functional inorganic materials using thin-film techniques. *MRS Bull.* **2002**, *27*, 301−308.
(52) Bezdek, J. C. *Pattern Recognition with Fuzzy Objective Function Algorithms*; Springer Science & Business Media, 2013.
(53) Nelson, A. Co-refinement of multiple-contrast neutron/X-ray reflectivity data using MOTOFIT. *J. Appl. Crystallogr.* **2006**, *39*, 273−276.

https://dx.doi.org/10.1021/acsaelm.0c00622
ACS Appl. Electron. Mater. 2020, 2, 3571−3576